Atmospheric Environment 336 (2024) 120746

Contents lists available at ScienceDirect

Atmospheric Environment

journal homepage: www.elsevier.com/locate/atmosenv

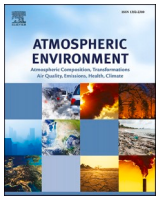

# Long-term observations of $NO_2$, $SO_2$, HCHO, and CHOCHO over the Himalayan foothills: Insights from MAX-DOAS, TROPOMI, and GOME-2

Prajjwal Rawat [a,*,1], Manish Naja [a,**], Mahendar C. Rajwar [a,b], H. Irie [c], Christophe Lerot [d,2], Mukesh Kumar [a], S. Lal [e]

[a] Aryabhatta Research Institute of Observational Sciences Manora Peak, Nainital, India
[b] DDU Gorakhpur University, Gorakhpur, 273009, India
[c] Center for Environmental Remote Sensing (CEReS), Chiba University, Japan
[d] Royal Belgian Institute for Space Aeronomy (BIRA-IASB), Brussels, Belgium
[e] Physical Research Laboratory, Navrangpura, Ahmedabad, India

## HIGHLIGHTS

- Foothill region showed NO2 diurnal variation of urban type with morning/evening peaks, while CHOCHO showed a noon maximum.
- Transport of air-masses significantly altered $SO_2$ and HCHO surface mixing ratios over the Himalayan foothill site.
- TROPOMI and GOME-2 underestimated the tropospheric $NO_2$ column by upto 48% compared to the MAX-DOAS observations.

## ARTICLE INFO

*Keywords:*
Air pollution
MAX-DOAS
Indo-gangetic plain
$NO_2$
$SO_2$
VOCs
Himalayan foothills

## ABSTRACT

Regional air pollution has become one of the utmost environmental concerns in India, especially over economically vibrant and densely populated regions, such as Northern India, including the Indo-Gangetic Plain (IGP). Additionally, the Himalayas adjacent to IGP provide conducive conditions to confine pollutants and transport them to greater horizontal and vertical extents. However, in-situ observations are sparse and limited over the Himalayas, where data retrievals from space-based sensors are fraught with difficulties. In light of this, observations of $NO_2$, $SO_2$, HCHO, and CHOCHO are made from a Himalayan foothills site (Pantnagar, 29.03° N, 79.47° E and 237 AMSL) utilizing remote sensing observation of Multi-AXis-Differential Optical Absorption Spectroscopy (MAX-DOAS). Data from TROPOspheric Monitoring Instrument (TROPOMI), and Global Ozone Monitoring Experiment-2 (GOME-2) satellite instruments are also presented. We investigate the temporal variations in near-surface mixing ratios, vertical profiles, and tropospheric columns of these trace gases from January 2017 to December 2020. The diurnal variation of $NO_2$ and HCHO at different altitude regions (surface to 3 km) were typically urban-type with morning and evening peaks. At the same time, the CHOCHO diurnal variation peaks in the noon hours. We observed annual mean tropospheric $NO_2$ vertical column densities (VCDs) of $3.2 \times 10^{15}$ (unit: molecules/cm$^2$), tropospheric $SO_2$ VCDs of $1.2 \times 10^{16}$, tropospheric HCHO VCDs of $1.6 \times 10^{16}$, and tropospheric CHOCHO VCDs of $0.6 \times 10^{15}$ from MAX-DOAS observations. MAX-DOAS comparison with the TROPOMI and GOME-2 VCDs shows an underestimation of up to 48% for satellite $NO_2$ VCDs, while $SO_2$ and HCHO VCDs show nominal biases in the range of 20–30%. The $R_{gf}$ sensitivity calculation shows prominent biogenic sources of VOCs during noon hours, while $R_{fn}$ calculation mostly shows a $NO_x$-limited ozone production regime over the Himalayan foothill site. The $R_{fn}$ monthly variations match reasonably well between the MAX-DOAS and TROPOMI, while $R_{gf}$ values were higher from satellite observations. This study highlights the factors governing the diurnal and monthly variation of different pollutants over the Himalayan foothill region and asses the space-borne observations for better utilization.

* Corresponding author.
** Corresponding author.
*E-mail addresses:* prajjwalrawat01@gmail.com (P. Rawat), manish@aries.res.in (M. Naja).
[1] Now at Langley Research Center, NASA, Hampton, 23,681, USA.
[2] Now at Constellr, Brussels, Belgium.

https://doi.org/10.1016/j.atmosenv.2024.120746
Received 15 April 2024; Received in revised form 17 July 2024; Accepted 6 August 2024
Available online 8 August 2024

## 1. Introduction

The rapid industrialization and fast-paced economic growth in many developing countries, particularly in South Asia, have accelerated the anthropogenic activities in the last few decades, leading to the degradation of air quality and climate (Akimoto, 2003; Li et al., 2017; Mauzerall and Wang, 2001). Poor air quality causes adverse effects on human health and agriculture and also degrades regional and global climate (McMichael et al., 2006; Patz et al., 2005; Ramanathan et al., 2001).

The Indo-Gangetic Plain (IGP), located south of the Himalayas, is one of the most densely populated and recognized pollution hotspots (Beig and Ali, 2006). The massive population surge across urban and suburban cities of IGP requires a larger demand for fossil fuels (FF) to meet their higher energy needs (Sinha et al., 2014). On the other hand, the rural populace tends to rely more on the combustion of solid biofuels (BF) (i.e., fuel-wood, crop residue, and dung cakes). Besides this, the extensive agricultural practices followed by residue burning over northern IGP is a significant source of several trace species, aerosols, and greenhouse gases in the regional atmosphere (Bhardwaj et al., 2016; Saud et al., 2011; Sharma et al., 2010; Van der Werf et al., 2017). Furthermore, the localized emissions and favorable meteorological conditions, coupled with the different regional and episodic emission sources, led to a drastic decline in the ambient air quality around the region and often reaches poor air quality standards (Ravishankara et al., 2020; Singh et al., 2018; Sinha et al., 2014). The IGP emission is further transported to the remote Himalayas via long-range transport, contaminating their pristine atmosphere (Kumar et al., 2010; Mallik & Lal, 2014; Naja et al., 2014).

Additionally, the unique geography of the IGP, with elevated slopes of the Himalayas on northern sites, enforces the accumulation of pollutants around the Gangetic-Himalayan foothills (Bhardwaj et al., 2018; Bonasoni et al., 2010). These pollutants undergo intensive mixing and frequent photochemical reactions and chemically transform into new compounds and secondary pollutants (Bianchi et al., 2021; Venzac et al., 2008). These are then transported into the free troposphere via convection and up-valley winds and redistributed globally (Ojha et al., 2017; Park et al., 2009). Hence, an improved understanding of sources and sinks of environmentally important gases over such foothill regions helps to understand the linkages between emission sources, chemical transformation, and their possible climatic alterations.

Nitrogen dioxide ($NO_2$) and sulfur dioxide ($SO_2$) are the most common primary pollutants among the inorganic gas pollutants, with emissions stemming from both human activities and natural sources. In addition to the inorganic primary pollutants many volatile organic compounds (VOCs) species come into the atmosphere from anthropogenic and biogenic sources and intensify the tropospheric chemistry with a larger potential for ozone and organic aerosol formation. The oxygenated volatile organic compounds (OVOCs) are a subset of VOCs, which are important precursors and intermediate products of atmospheric photochemical reactions. At the same time, possible retrieval from the space-borne sensor helps to monitor the OVOCs or track VOCs on a greater spatial and temporal scale.

More specifically, $NO_2$, a toxic nitrogen-containing pollutant, comes mainly from fossil fuels and biomass burning and plays a vital role in forming photochemical smog and is a major precursor of various secondary pollutants like tropospheric ozone and nitrate aerosols (Gilbert et al., 2003). Where $SO_2$, a common sulfur oxide, is a primary pollutant mainly emitted from natural sources (i.e., volcanic eruptions) and anthropogenic sources, including coal, diesel, and gasoline (Chen et al., 2007; Naja et al., 2014). Recently, India has emerged as a global $SO_2$ emitter and has overtaken Chinese $SO_2$ emissions (Li et al., 2017); hence, long-term $SO_2$ observations are essential in India. Additionally, formaldehyde (HCHO) and glyoxal (CHOCHO) are important OVOCs, which plays vital roles in tropospheric chemistry and Secondary Organic Aerosols (SOAs) formation and act as tracers of VOCs oxidation (Kim et al., 2010; Koppmann et al., 2005; Volkamer et al., 2007). Most of the global glyoxal burden comes from biogenic sources like isoprene and monoterpene oxidation (Fu et al., 2009), while formaldehyde is predominantly produced from the oxidation of methane with smaller biogenic and direct emissions (Henry et al., 2012; Vrekoussis et al., 2009).

So far, only a few continuous MAX-DOAS observations have been established over the IGP region (Hoque et al., 2018a; Kumar et al., 2020), apart from one campaign-based mobile MAX-DOAS observation (Shaiganfar et al., 2011). MAX-DOAS observation by Kumar et al. (2020) found that the northern IGP site Mohali is less polluted than Chinese and Western countries on the urban and suburban $NO_2$ scale but comparable on the HCHO scale with no notable trend in these trace gases for the four-year observations (2013–2017). Both Kumar et al. (2020) and Shaiganfar et al. (2011) compared the OMI $NO_2$ tropospheric column with MAX-DOAS VCDs observations over Mohali and Delhi sites and found reasonable agreements with notable lower columns (~30%) of OMI.

Hoque et al. (2018a) also discussed the one-year (2017) near-surface observation of HCHO and CHOCHO over Pantnagar from MAX-DOAS. Here, we have carried out four years (2017–2020) observations of $NO_2$, $SO_2$, HCHO, and CHOCHO using MAX-DOAS over Pantnagar, a semi-urban Himalayan foothill site in the northern IGP. We discuss diurnal variations and vertical profiles of these pollutants for four years with a detailed discussion on the factors influencing their ambient levels and sources that have been missing in the previous studies. Further, we have included the observations from afternoon and morning overpass satellite TROPOMI and GOME-2, respectively, and discussed their possible differences with MAX-DOAS. We have used the histograms remainders, Gaussian fitting, and correlation techniques to describe the corresponding differences. Furthermore, the possible sources of OVOCs coupled with MODIS enhanced vegetation index (EVI) and ozone production regime are also presented.

## 2. Study region, dataset, and methodology

### 2.1. Study region and general meteorology

Measurements were conducted from January 2017 to December 2020 using state-of-the-art MAX-DOAS instruments at the Biotech Bhavan, Biotechnology Council, Department of Agriculture, Haldi, Pantnagar ($29.0^0$ N, $79.5^0$ E, 237 m AMSL). Fig. 1 shows the geographical map of northern India and the location of the observation site (Red balloon) with regridded TROPOMI observation of $NO_2$ and CHOCHO VCDs at $0.5^{\circ} \times 0.5^{\circ}$ spatial resolution during May 2019 (Lerot et al., 2021; van Geffen et al., 2020) in the right. There are no major emission sources in the vicinity of the observational site except the local vehicular and biogenic emissions. In the nearby Pantnagar, some small-scale industries are located in Rudrapur ~12 km southwest and Haldwani ~25 km northeast. In contrast, at ~225 km west, the most polluted metropolitan city, Delhi, is located. The TROPOMI $NO_2$ observations (Fig. 1a) also show higher levels of $NO_2$ around the west direction of Pantnagar emerging from pollution hotspots that are often transported to the nearby regions (Srivastava et al., 2021). The IGP region is a source of many pollutants in the central Himalayas including VOCs (Rajwar et al., 2024). Still, the dense Himalayan forest with widely distributed oaks and pine trees, significantly contributes to the biogenic emission in the local environment (Bianchi et al., 2021), which is also observed in the TROPOMI CHOCHO observations (Fig. 1b).

Furthermore, we have utilized data from ERA-5 meteorological parameters, including total radiation, MODIS fire counts, and MODIS EVI (250 m spatial and 16 days temporal resolution) to better describe the sources and meteorological influences on trace gases. The variation in meteorological conditions and solar radiation heavily decides the local chemistry and abundance of pollutants. Hence, the monthly and diurnal variation of various meteorological and radiation fields based on ERA-5 reanalysis data from January 2017 to December 2020 over Pantnagar is

also studied and shown in Fig. 2. Monthly variations of the boundary layer (BL) height, the temperature at 2m above ground (T2m), and surface solar radiation (SSR) show higher values during spring and summer. In contrast, the wind speed and total precipitation (TP) show clear maxima for the summer-monsoon. The diurnal variation shows higher BL, SSR, and T2m during the noon hours, while total precipitation and wind show relatively higher values in the afternoon and late morning hours (Fig. 2a). Based on such variations, Indian seasons are broadly categorized as follows: winter (December, January, and February), spring (March, April, and May), summer-monsoon (June, July, and August), and autumn (September, October and November) (Ojha et al., 2012).

### 2.2. MAX-DOAS observations

MAX-DOAS, a compact, low-cost, and low-power remote sensing instrument, is a state-of-the-art effective ground-based remote sensing instrument for measuring the vertical distribution and columnar concentrations of tropospheric trace gases (i.e., $NO_2$, $SO_2$, HCHO, and CHOCHO) and aerosol extinction coefficient from spectra of scattered sunlight recorded at multiple elevation angles (Hönninger et al., 2004; Irie et al., 2015, 2019; Wagner et al., 2004). Trace gases and aerosol observations from MAX-DOAS have increased considerably in recent years worldwide (Hoque et al., 2018b; Irie et al., 2011, 2015; Peters et al., 2012). The increasing use of MAX-DOAS due to automatic operation and the availability of vertical profiles are the advantages of this instrument with simultaneous and synergic observations and often utilized over the Asian region (Kumar et al., 2020; Hoque et al., 2018a, 2018b; Biswas & Mahajan, 2021). The limitation of MAX-DOAS is the power failure and optically-thick-cloudy/rainy weather when data retrieval and observation get interrupted.

The MAX-DOAS instrument measures UV–visible spectra of scattered sunlight (between 310 and 515 nm with spectral resolution of about 0.4 nm) at several elevation angles (ELs), i.e., 3°, 4°, 5°, 6°, 8°, and 70°, and the same sequence of ELs is repeated every 15 min. Observed spectra are analyzed using our retrieval algorithm, JM2 (Japanese MAX-DOAS profile retrieval algorithm, version 2) (e.g., Irie et al., 2008a; Irie et al., 2011; Irie et al., 2015). The observed solar spectra are analyzed utilizing the Differential Optical Absorption Spectroscopy (DOAS) fitting technique (Hönninger and Platt, 2002; Platt and Stutz, 2008) to calculate the differential slant column density (ΔSCD). The DOAS fitting window of $NO_2$, $SO_2$, HCHO, and CHOCHO is given in Table S1 which is utilized to obtain respective ΔSCD. An optimal estimation method is used together with a lookup table (LUT) for the box air mass factor (Abox), which is calculated by the JACOSPAR RTM (Irie et al., 2015) and used to converted SCDs to their respective VCDs and vertical profiles. Also, the MAX-DOAS instruments have taken part in the different CINDI campaigns and reported reasonable SCDs and VCDs retrieval compared to other DOAS (Tirpitz et al., 2020). The detailed description of instruments, retrieval procedures and error estimates are described in Irie et al. (2008a, 2008b, 2011 and 2015) and described briefly in supplementary S1.1.

### 2.3. TROPOMI/S–5P and GOME-2/MetOp-b trace gases column observations

TROPOMI, onboard Sentinel-5 Precursor (S–5P), is a sun-synchronous polar-orbiting satellite, with a swath width of 2600 km and 13:30 local time ascending node. It is launched on October 13, 2017) with push-broom imaging spectrometer providing dedicated measurements of atmospheric composition with a pixel resolution of 3.5 km × 5.5 km (3.5 km × 7 km before August 2019) at Nadir (Veefkind et al., 2012). The instrument measures UV–Vis spectra with a spectral resolution of about 0.5 nm to enable trace gases retrieval (Griffin et al., 2019; Theys et al., 2017). We have used TROPOMI offline level-2 data of better quality (qa_value > 0.75) for tropospheric VCDs observation of

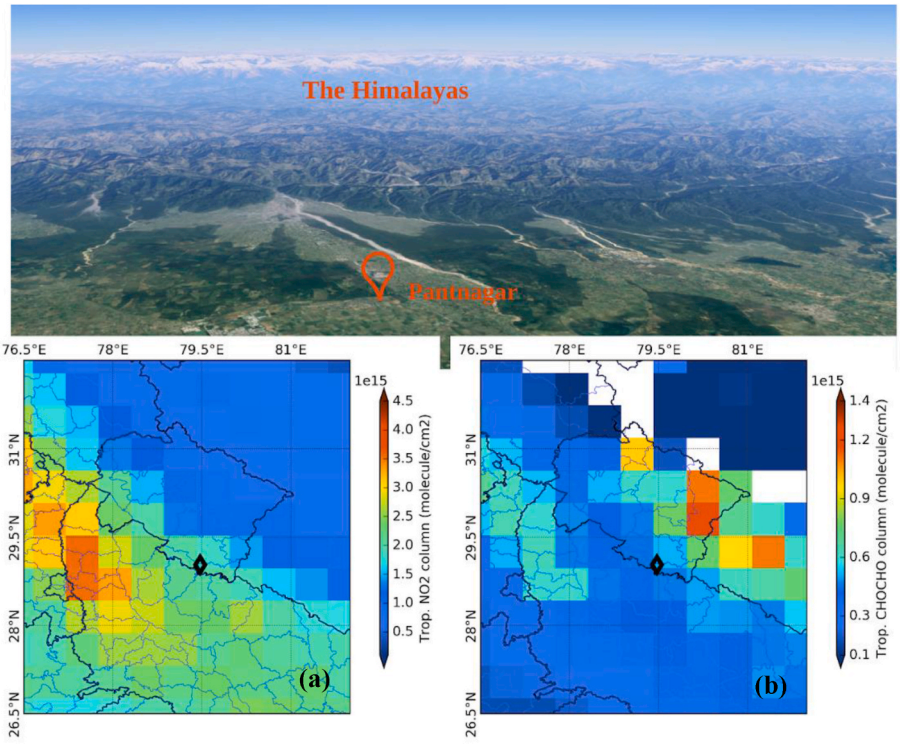


**Fig. 1.** The Himalayas and foothill region with MAX-DOAS observation location (Pantangar) shown as the red balloon over the northern India (© Google earth). TROPOMI retrieved **(a)** $NO_2$ and **(b)** CHOCHO average VCDs at 0.5° × 0.5° spatial resolution around the Pantnagar site during May 2019 is also shown. The marked black diamond shows the location of Pantnagar, where MAX-DOAS observations were performed. Indian state (black line) and district (blue line) boundaries are also inculcated in the bottom map.

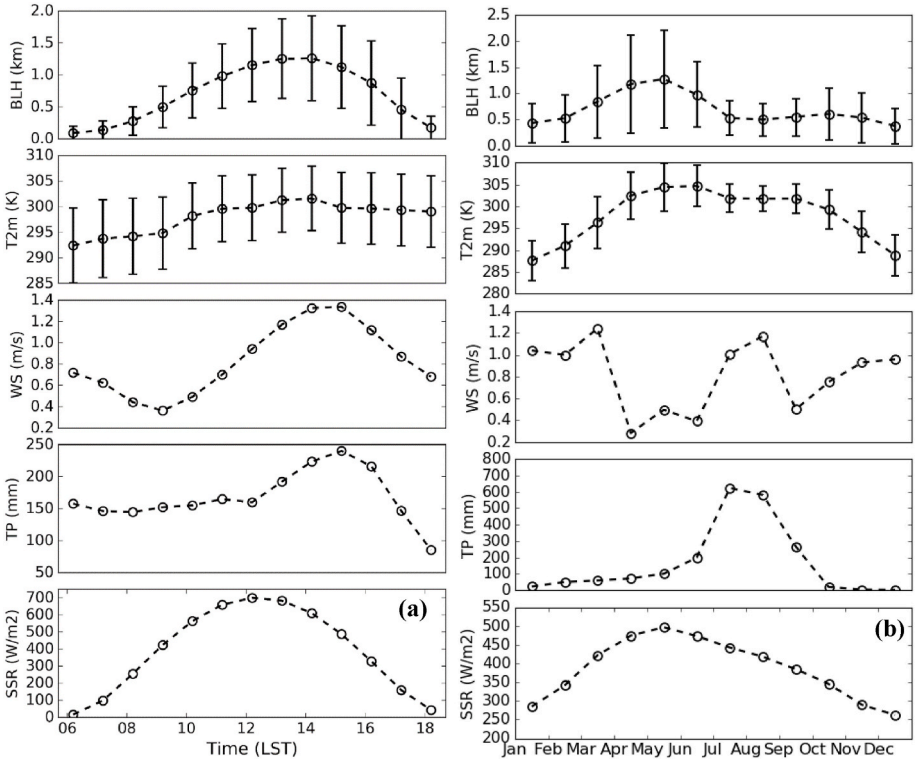


**Fig. 2.** (a) Diurnal and **(b)** monthly variation of meteorological parameters (boundary layer height, temperature (2m), wind speed, total precipitation and SSR) over Pantnagar based on ERA-5 reanalysis data during 2017–2020.

$NO_2$, $SO_2$, and HCHO from May 2018 to December 2020 and January 2018 to December 2020 for CHOCHO (Lerot et al., 2021). The retrieval of trace gases VCDs from TROPOMI measured nadir radiance and solar irradiance spectra are explained elsewhere (Griffin et al., 2019; Lerot et al., 2021; Theys et al., 2017; Veefkind et al., 2012; Vigouroux et al., 2020) and discussed briefly in supplementary se ction S1.2.

The GOME-2, flying on the MetOp series of satellites and launched on September 17, 2012 (MetOp-b), into sun-synchronous orbit with an equator crossing time of 0930 h (Burrows et al., 1999; Munro et al., 2016). It is a nadir-scanning UV-VIS spectrometer (240 and 790 nm range) with FWHM between 0.26 nm and 0.51 nm (spectral resolution). It is a scanning instrument with a coaster spatial resolution of 80 × 40 $km^2$ at nadir. We have utilized the level-2 data of GOME-2b for column amounts of $NO_2$, $SO_2$, HCHO, and CHOCHO during the four-years from 2017 to 2020, where $NO_2$ is a tropospheric column and others are the total column. The retrieval of trace gases VCDs from GOME-2 are explained elsewhere (Burrows et al., 1999; De Smedt et al., 2012; Richter and Burrows, 2002; Spurr et al., 2010; Valks et al., 2011) and discussed briefly in supplementary s ection S1.3.

## 3. Results and discussions

### 3.1. MAX-DOAS observations of $NO_2$, $SO_2$, HCHO, and CHOCHO

#### 3.1.1. Monthly variations in 0–1 and 1–3 km layers

We analyze the mixing ratios near the surface in the 0–1 km layer and adjacent layer (1–3 km) and their percentage differences. Fig. 3 shows the average monthly variations in $NO_2$, $SO_2$, HCHO, and CHOCHO observed at the foothill IGP site (Pantnagar) for years between 2017 and 2020 within 0–1 km and 1–3 km layer. $NO_2$ shows a typical urban monthly variation with higher mixing ratios during winter-spring and lower mixing ratios during the summer-monsoon for the near surface layer (Fig. 3a). While monthly variation in the adjacent layer (1–3 km) is mostly constant with a significant drop in mixing ratios by more than 85%. The higher mixing ratios near the surface during winter and spring could be interpreted as regional emissions from vehicular and small-scale industries coupled with higher biomass burning (Fig. S1) and a longer lifetime of $NO_2$ during the period (Beirle et al., 2003; Bhardwaj et al., 2016; Ghude et al., 2008; Jena et al., 2015). However, the summer lows can be attributed to monsoonal washout/deposition of pollutants, the arrival of clean oceanic air masses, and larger oxidations of $NO_2$ via OH (Wang and Jacob, 1998). The annual average $NO_2$ mixing ratio in the 0–1 km layer was 1.17 ± 0.03 ppbv. During different seasons highest $NO_2$ mixing ratios are observed in winter (1.37 ± 0.05 ppbv) and the lowest in summer-monsoon (0.90 ± 0.03 ppbv).

The monthly variation of $SO_2$ is shown in Fig. 3b. The average $SO_2$ mixing ratio over the foothill IGP site in the lowest 0–1 km layer during 2017–2020 is 3.2 ± 0.7 ppbv, and the observed seasonality of $SO_2$ shows slightly higher values during autumn, 3.52 ± 0.8 ppbv and lower during winter 2.95 ± 0.7 ppbv (Table 1), and similar seasonality is also followed by 1–3 km layer with lower mixing ration by 60–70% compared to 0–1 km layer. The higher values during autumn were also observed in surface observations, reported earlier over nearby (~65 km away to Pantnagar) town Nainital, and the regional emissions, transport, and relatively lower oxidant/wet scavenging after lesser humidity under shallower boundary layer during autumn was explained as the possible reason for such higher $SO_2$ (Igarashi et al., 2006; Naja et al., 2014).

Fig. 3c shows the monthly variation of HCHO in the 0–1 km and 1–3 km layers. The HCHO monthly variations show bimodal variation with two enhancement periods during spring and autumn, which are intense biomass-burning periods (Fig. S2). The average HCHO mixing ratio near the surface during the observation period over the foothill IGP site was 4.8 ± 1.03 ppbv. The observed HCHO mixing ratios near the surface are relatively higher than earlier reported values over the IGP region (1.4 ± 1.0 ppbv) based on WRF-Chem simulation (Chutia et al., 2019), while MAX-DOAS observation over Mahabaleshwar and Pune, the western Indian sites shows similar HCHO observation in the range of 0.16 ppbv–4.8 ppbv and 0.3 ppbv–10.6 ppbv respectively (Biswas &

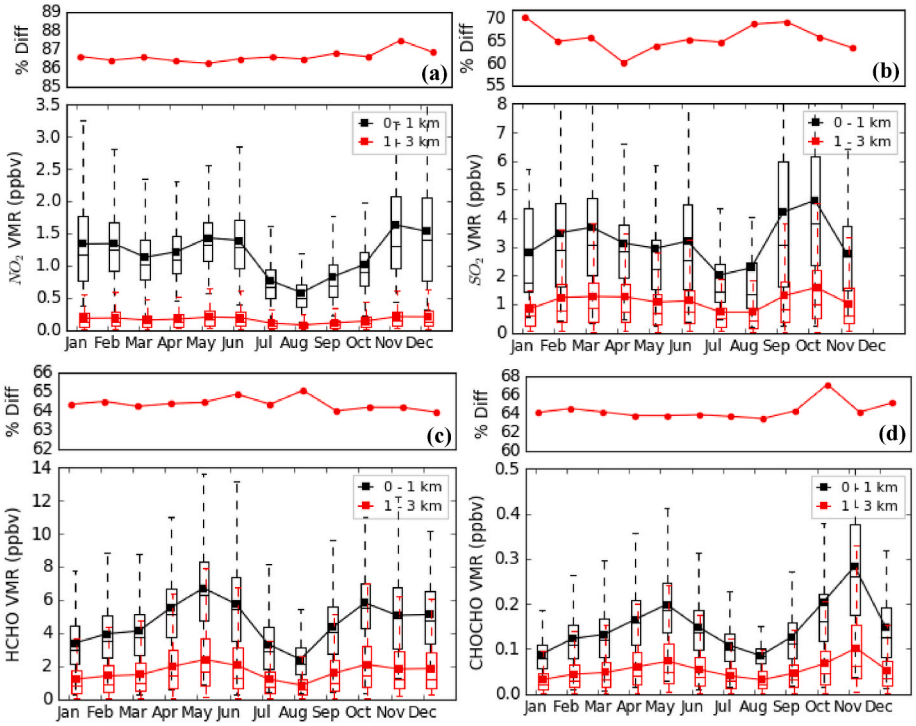


**Fig. 3.** Monthly variations of retrieved **(a)** $NO_2$, **(b)** $SO_2$, **(c)** HCHO, and **(d)** CHOCHO from MAX-DOAS in 0–1 km and 1–3 km layer during 2017–2020 over Pantnagar. Percentage difference between the two adjacent layers is also shown in the top panel for $NO_2$, $SO_2$, HCHO, and CHOCHO gases, respectively.

**Table 1**
Mixing ratios of $NO_2$, $SO_2$, HCHO, and CHOCHO from MAX-DOAS in 0–1 km layer at the foothill IGP site during four seasons averaged for 2017–2020.

| Gases/ Seasons | Winter (ppbv) | Spring (ppbv) | Summer-Monsoon (ppbv) | Autumn (ppbv) |
|---|---|---|---|---|
| $NO_2$ | 1.47 ± 0.05 | 1.23 ± 0.04 | 0.90 ± 0.03 | 1.1 ± 0.03 |
| $SO_2$ | 2.95 ± 0.7 | 3.05 ± 0.7 | 3.20 ± 0.7 | 3.52 ± 0.8 |
| HCHO | 4.05 ± 0.9 | 5.35 ± 1.1 | 4.09 ± 0.8 | 5.71 ± 1.3 |
| CHOCHO | 0.11 ± 0.03 | 0.16 ± 0.03 | 0.12 ± 0.03 | 0.23 ± 0.06 |

Mahajan, 2021; Biswas et al., 2020). The adjacent layer also followed a similar monthly variation with mixing ratios lower by about 65%.

The highest HCHO mixing ratio over the foothill IGP site is observed during autumn (5.71 ± 1.3 ppbv) and the lowest during winter (4.05 ± 0.9 ppbv), shown in Table 1. Additionally, the biogenic emissions might also increase HCHO concentrations around the Himalayan foothill regions (Surl et al., 2018). Analysis of MODIS EVI shows higher values during the autumn seasons over the foothill IGP site, discussed later in section 3.6, which significantly contributes to higher levels of HCHO during autumn under a shallow boundary layer, in addition to biomass burning. Like HCHO, CHOCHO also shows higher values during autumn in the range of 0.2 ppbv–0.7 ppbv (Fig. 3d). The annual average CHOCHO mixing ratio in the 0–1 km layer was 0.16 ± 0.03 ppbv, with the highest values during autumn (0.23 ± 0.06 ppbv) and lowest during winter (0.11 ± 0.03 ppbv) in 0–1 km layer (Table 1). The CHOCHO monthly variation in 1–3 km layer was similar to the surface layer, with values lower by 65%, additionally the largest vertical drop of trace gases is observed for $NO_2$ mixing ratios in the range of 86–88% and more details on the monthly vertical profile is discussed in s ection 1.1.3.

### *3.1.2. Diurnal variations in 0–1 and 1–3 km layers*

Fig. 4 shows the diurnal variation of $NO_2$ and $SO_2$ from MAX-DOAS observations in the 0–1 and 1–3 km layers during different seasons for the observational period (2017–2020). The average mixing ratios of $NO_2$ during the morning (06:00–10:00 IST), noon (11:00–14:00 IST), and evening (15:00–18:00 IST) hours were 1.31 ± 0.07 ppbv, 0.97 ± 0.05 ppbv, and 1.45 ± 0.07 ppbv respectively (Fig. 4a) in 0–1 km. The maximum mixing ratio of $NO_2$ near the surface during morning and evening hours is possibly due to rush-hour vehicular emissions and a shallower boundary layer. Additionally, freshly emitted NO could react with $O_3$ and produce more $NO_2$ during lower solar radiation. However, higher solar radiation could effectively photolysis and oxidize $NO_2$ within deeper boundary layers during the noon hours. Such diurnal variation is also followed consistently at higher altitudes (1–3 km) with a larger standard deviation, possibly due to the lower sensitivity of MAX-DOAS at higher altitudes. Among the seasons stronger diurnal features were observed in autumn, while winter showed relatively weaker variations. Further, The $SO_2$ diurnal variation shows a morning hour build-up and successive decrease at a lower rate during the noon and the evening hours in different altitudes of the lower troposphere (Fig. 4b). The average near surface mixing ratio of $SO_2$ during the morning, noon, and evening hours were 1.9 ± 0.6 ppbv, 2.0 ± 0.6 ppbv, and 1.4 ± 0.4 ppbv, respectively. The levels were higher during autumn and relatively lower during summer months. Measurements revealed a clear diurnal cycle for the trace gases, which seems to be derived from factors like local emissions, meteorological variations, and chemistry.

Fig. 5 shows the diurnal variation of HCHO and CHOCHO from MAX-DOAS observations in the 0–1 and 1–3 km layers during different seasons. The average HCHO during the morning, noon, and evening hours were 4.9 ± 1.0 ppbv, 4.5 ± 0.9 ppbv, and 5.6 ± 1.0 ppbv, respectively in 0–1 km. Though HCHO shows a clear seasonal cycle, its diurnal variation is relatively weaker and shows lesser photochemical activities (Fig. S3). In general, higher HCHO mixing ratios are observed during the evening and morning hours and lower during the noon hours (Fig. 5a). The production of HCHO is mainly controlled by methane and VOCs oxidation in the availability of $NO_x$ (Lowe & Schmidt, 1983). Its removal processes are photo-dissociation to carbon monoxide (CO) in the presence of hydroxyl radical (OH), which is higher during noon hours (Volkamer et al., 2007).

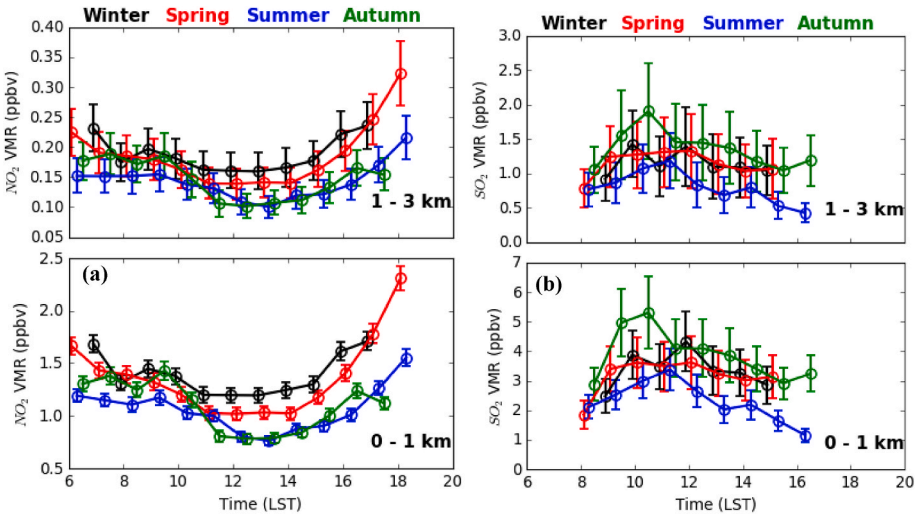


**Fig. 4.** Average diurnal variations of retrieved **(a)** $NO_2$ and **(b)** $SO_2$ from MAX-DOAS observations in 0–1 and 1–3 km layers during 2017–2020. Seasons are shown with different color.

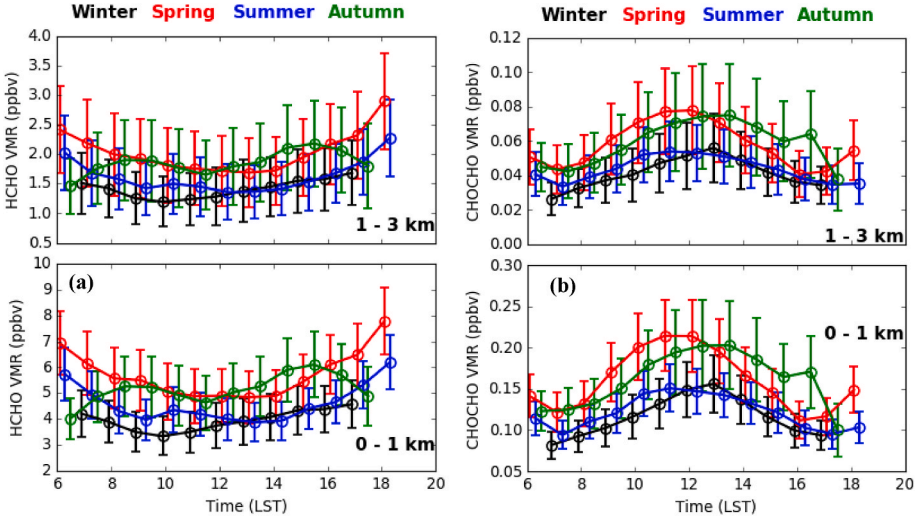


**Fig. 5.** Average diurnal variations of retrieved **(a)** HCHO and **(b)** CHOCHO from MAX-DOAS in 0–1, 1–3 km layers during 2017–2020. Seasons are shown with different color.

Fig. 5b shows the diurnal variation for CHOCHO over the foothill IGP site. The average CHOCHO during the morning, noon, and evening hours were 0.13 ± 0.03 ppbv, 0.17 ± 0.04 ppbv, and 0.12 ± 0.03 ppbv, respectively near the surface. A relatively higher CHOCHO during noon hours is observed when higher temperature induces higher biogenic emissions. Biogenic emissions of isoprene and monoterpenes significantly increase as a response to an increasing temperature and solar radiation and contribute to higher CHOCHO production (Surl et al., 2018; MacDonald et al., 2012). The diurnal variation in the percentage rate of change (Fig. S3) of these trace gases is also studied for different altitudes, and more or less identical photochemical activity is observed for all seasons, with relatively higher activities for autumn and spring. In the case of HCHO, the loss and production mechanism during autumn seems different from the rest of the seasons.

Additionally, the diurnal cycle of $NO_2$, HCHO, and CHOCHO over Chongqing, southwest China (Xing et al., 2020) shows a similar diurnal variation for $NO_2$ and HCHO as measured over the foothill IGP site, while CHOCHO shows a completely different diurnal variation with noon minima over southwest China compared to Pantnagar. Also, the diurnal variation of the $SO_2$ vertical profile over Hefei, East China (Hong et al., 2021) shows higher concentrations during the early morning and late evening hours, which is different from the $SO_2$ observations over Pantnagar (Fig. 4b). The possible reasons for such differences could be different sources (anthropogenic or biogenic), meteorology, and the geography of these regions.

### 3.1.3. *Monthly vertical distribution in the lower troposphere (0–3 km)*

Fig. 6 shows the average monthly vertical distribution of the $NO_2$, $SO_2$, HCHO and CHOCHO in the lower troposphere (0–3 km) obtained from the MAX-DOAS observations. The $NO_2$, $SO_2$, HCHO, and CHOCHO mixing ratio profiles have a very identical variation, with most of the concentration of these gases within the boundary layer (BL). This is quite obvious since most of the sources for these trace gases are close to the surface, while an abrupt decrease can be seen with altitude. The top left Fig. 6 shows the monthly variation of the $NO_2$ vertical profile. Higher $NO_2$ concentrations (~1 ppb) can be seen near the surface during most of the season except during the summer-monsoon, where an apparent reduction of the $NO_2$ vertical profile is observed.

The monthly variation of the $SO_2$ vertical profile (Fig. 6, top right) shows higher concentrations during autumn and a clear drop in

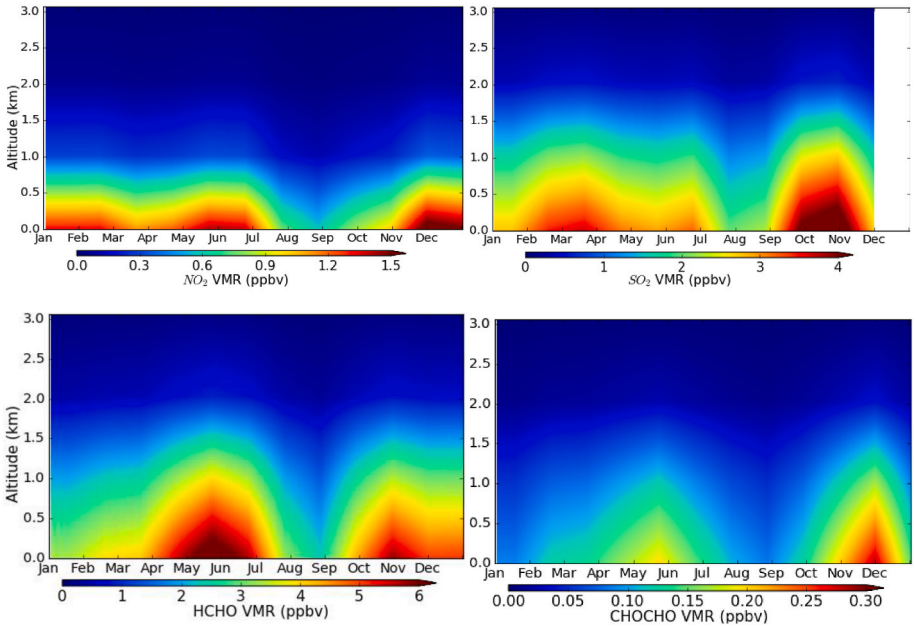


**Fig. 6.** Average monthly (2017–2020) variations of the vertical profile of $NO_2$, $SO_2$, HCHO, and CHOCHO from MAX-DOAS observations in 0–3 km altitudes over Pantnagar.

monsoons. Further $SO_2$ vertical gradient with altitude was relatively lower as compared to $NO_2$. The monthly variation of the HCHO vertical profile (Fig. 6 bottom left) shows a clear increase during the spring and autumn when the biomass burning event over northern India increases (Fig. S1). The monthly variation of the CHOCHO vertical profile (Fig. 6 bottom right) shows a higher increase during autumn than during the spring. As discussed below, this is related to the EVI over Pantnagar, which is higher (~35%) during autumn (~0.35) than during the spring (~0.26).

The summer-monsoon minimum is consistent for all gases as during the monsoon; there is the arrival of clean oceanic air and wet removal of local pollutants (total precipitation was higher than 500 mm over Pantnagar, Fig. 2). However, the higher mixing ratios, even in deeper boundary layers during the spring season, show the influence of local emission, larger photochemistry (larger solar radiation of >450 $Wm^{-2}$, Fig. 2), and contribution from local sources like agricultural residue burning from the Punjab and Haryana region (Fig. S2).

### 3.2. Seasonal frequency distributions and role of winds

Fig. 7 shows the frequency distribution of $NO_2$, $SO_2$, HCHO, and CHOCHO in the 0–1 km layer for different seasons and corresponding wind rose diagrams for respective seasons in the insects. As there were no simultaneous meteorological measurements over the observation site, we have utilized the ERA-5 derived wind speed and wind directions at 10m above the surface (Belmonte Rivas & Stoffelen, 2019). Similar corroboration of surface-based wind and surface pollutants are also used in other studies (Lin et al., 2008; Mallik et al., 2015). The collocated and concurrent hourly values between ERA-5 reanalysis and MAX-DOAS observations are then utilized for analysis.

The frequency distribution analysis shows the populated mixing ratio (0–1 km) of $NO_2$, $SO_2$, HCHO and CHOCHO are around 1.2 ppbv, 4 ppbv, 6 ppbv and 0.25 ppbv, respectively, during the spring and are mostly higher or comparable to other seasons. The wind rose diagram shows a significant dependence of these gases with winds and has few preferential wind direction sectors. During spring and autumn months, the points are mostly distributed around the $170^0$ and $180^0$ directions, when the prevailing wind from the northwestern direction like Delhi, Punjab, and other potential sources region (Fig. S4), where higher fire counts are observed (Fig. S1), can contribute to the ambient levels of pollutants over the foothill IGP site and nearby Himalayas (Kumar et al., 2010; Ojha et al., 2012). While during the winter and summer-monsoon periods, apart from the western contribution, notable points are also distributed in the $315^0$ to $360^0$ sector and show influences from south-eastern IGP plains. Further, a higher concentration of $NO_2$ and CHOCHO was mostly around the low wind speed sectors, implying their sources are predominantly localized and anthropogenic (Fig. 7a–d). In comparison, $SO_2$ and HCHO show higher concentrations even for high wind speed (~6 m/s) and exhibit the possible role of long-range transport (Fig. 7b and c).

### 3.3. Comparison of MAX-DOAS VCDs with TROPOMI and GOME-2 observations

The space-based observation (i.e., GOME, OMI, and TROPOMI) has increased recently to characterize the global distributions, emission sources, and trends of various trace gases, including interpreting surface air quality (Long et al., 2022; Wang et al., 2021; Zhu et al., 2023); however, their assessment with ground-based instruments is necessary to understand their retrieval. Fig. 8 shows the histogram reminder between the satellite retrieved VCDs and the MAX-DOAS observations with their mean biases and standard deviations. The appropriate bin width and bin number for each distribution are calculated based on the Freedman-Diaconis rule. The Histogram remainders are the concurrent and collocated VCDs differences of MAX-DOAS with the TROPOMI and GOME-2. In general, underestimation is observed in the case of $NO_2$ ($-1.23 \times 10^{15}$ and $-2.01 \times 10^{15}$ molecule/$cm^2$) and $SO_2$ ($-0.01 \times 10^{16}$ and $-0.06 \times 10^{16}$ molecule/$cm^2$) by both the space-based instruments (TROPOMI and GOME-2) in comparison with MAX-DOAS (Fig. 8a and b). At the same time, TROPOMI observation for HCHO and CHOCHO VCDs show relatively smaller low bias, while GOME-2 largely overestimates CHOCHO by more than 70% (Fig. 8d).

Further, it can be noticed that the mean and the standard deviation of the distribution are lower for TROPOMI compared to coarser resolution GOME-2. A Gaussian distribution function was utilized to fit the remainders for a smoother interpretation that shows the random errors in VCDs measurements are normally distributed. Previously it has been reported the MAX-DOAS VCDs of $NO_2$, HCHO, and CHOCHO have been

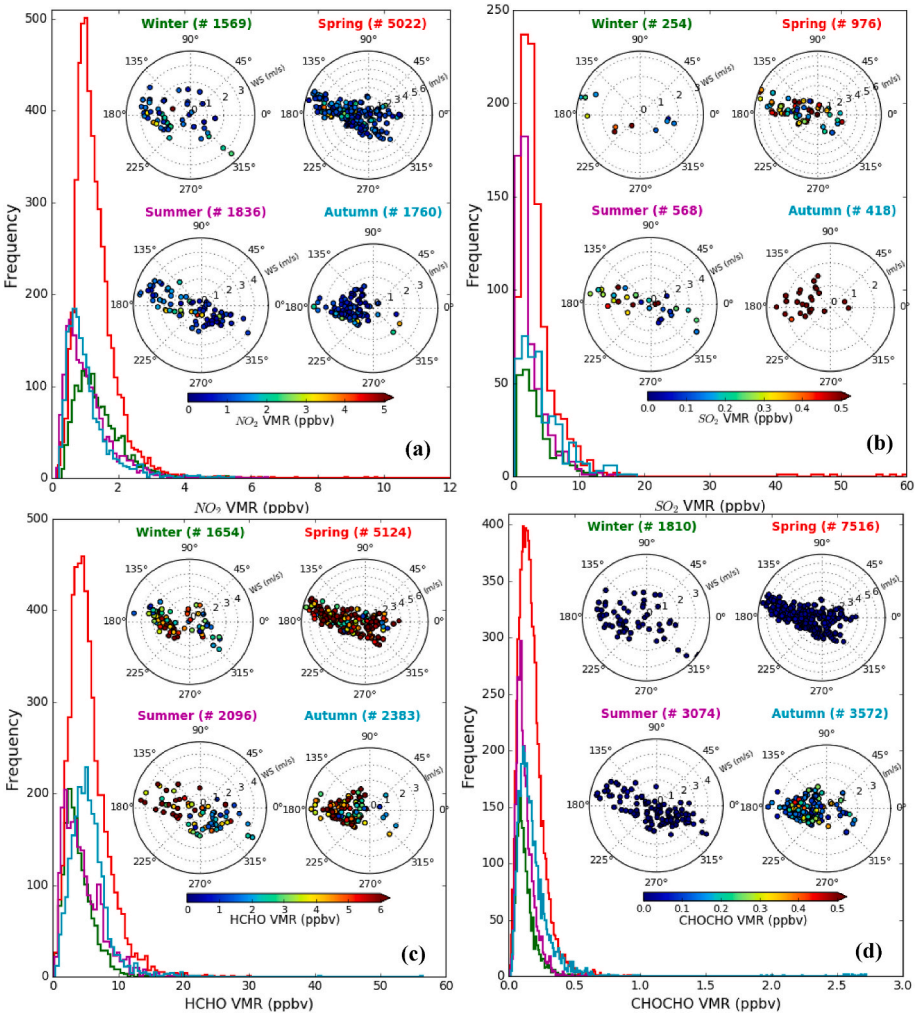


**Fig. 7.** Seasonal frequency distribution of **(a)** $NO_2$, **(b)** $SO_2$, **(c)** HCHO, and **(d)** CHOCHO from MAX-DOAS in 0–1 km during 2017–2020. Wind rose diagrams and corresponding mixing ratios of trace gases are also shown in insects. The wind speed (m/s) is also given at different radial locations and the different radial angles like $0^{\circ}$, $90^{\circ}$, $180^{\circ}$, and $270^{\circ}$ show east, north, west, and south directions (mathematical angle), respectively.

higher compared to the TROPOMI observations by more than 40% (De Smedt et al., 2021; Lerot et al., 2021; Verhoelst et al., 2021). Here the mean biases with the appropriate reminder distribution for a longer time period is presented with relatively loose collocation and shows similar underestimation for satellite $NO_2$ VCDs.

Further, to check how the two different instruments relate to the common observational features of VCDs, the correlation coefficient is calculated for the monthly averaged data. For $NO_2$ and HCHO, a reasonable correlation is seen between the satellite and ground-based observations, whereas in the case of $SO_2$ and CHOCHO, a poor correlation is observed (Fig. 8a–d). The corresponding linear regression slopes are 0.21 (0.43) and 0.47 (0.25) for $NO_2$ (HCHO) for TROPOMI/MAX-DOAS and GOME-2/MAX-DOAS, respectively and intercepts of $1.2 \times 10^{15}$ ($0.48 \times 10^{16}$) and $1.8 \times 10^{15}$ ($1.4 \times 10^{16}$) molecule/cm$^2$. We have also checked the correlation during the low and high pollution periods; still, no notable improvements in correlation were seen. However, it should be noted that MAX-DOAS and satellite measurements are not synchronized. Differences in measuring time, vertical sensitivity, spatial coverage, retrieval methodology and input a-priories could probably introduce systematic biases in the satellite VCDs and MAX-DOAS. More specifically, satellite observations do not fully resolve horizontal gradients near intense emission sources but rather smooth out these gradients by averaging over adjacent regions, known as the gradient smoothing effect. Whereas, the varying altitude profiles of gases (i.e., $NO_2$) and aerosols used for AMF calculations further introduce systematic discrepancies in the tropospheric vertical column densities (VCDs) retrieved by satellite instruments. In contrast, MAX-DOAS observations are minimally impacted by these factors. Also, space-based instruments have limited sensitivity close to the ground, where MAX-DOAS shows the highest sensitivity (Irie et al., 2008a; Kanaya et al., 2014).

### 3.4. Monthly variations in $NO_2$, $SO_2$, HCHO, and CHOCHO VCDs from TROPOMI and GOME-2

Fig. 9 shows the monthly variation in VCDs of $NO_2$, $SO_2$, HCHO, and CHOCHO from TROPOMI (afternoon overpass) and GOME-2 (morning overpass) satellite observation over the foothill site (Pantnagar) during 2017–2020. In the case of TROPOMI, more recent observations based on its availability are utilized (Fig. S5). MAX-DOAS observations close to satellite overpass timings of GOME-2 and TROPOMI are also shown with green color. For the spatial and temporal collocation, 80 × 100 km box around Pantnagar (coarser collocation to increase matchups and homogeneous region for both the satellite) and ±2 h overpass is used. The concentration levels and monthly variation of most trace gases were relatively in agreement with satellite and MAX-DOAS observations, with some positive and negative biases discussed in section 3.3.

Both the satellite observations reasonably captured a systematic monthly variations of $NO_2$ and HCHO with higher columns during winter-spring and lower during the summer-monsoon (Fig. 9). However,

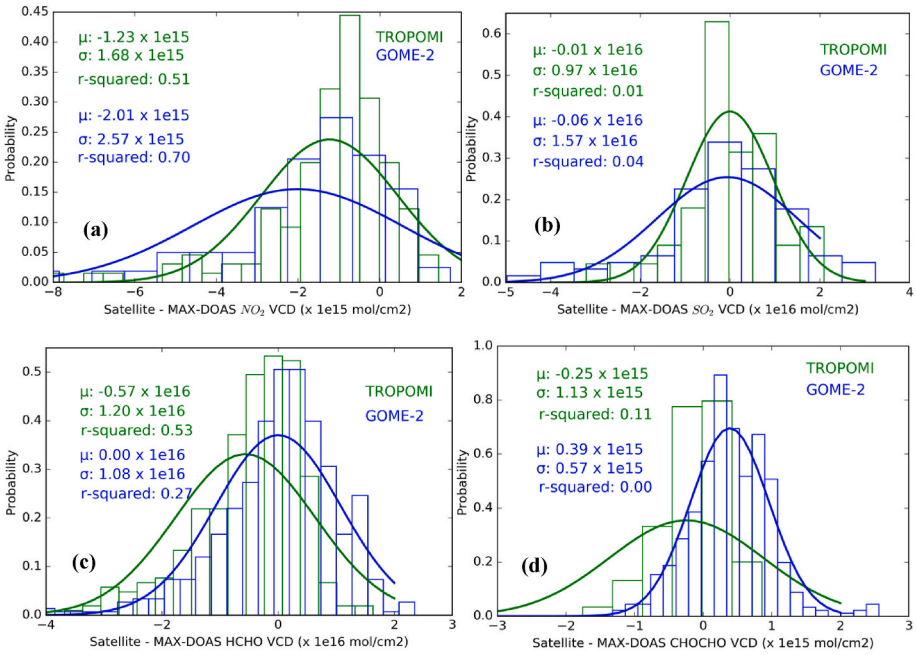


**Fig. 8.** Histograms showing the remainders between TROPOMI/MAX-DOAS and GOME-2/MAX-DOAS retrieved **(a)** $NO_2$, **(b)** $SO_2$, **(c)** HCHO, and **(d)** CHOCHO columns over Pantnagar. The Y-axis shows the area-averaged probability. The fitted Gaussian distribution is plotted as a black curve. μ and σ denote the mean and standard deviation in molecule/cm$^2$ of the fitted Gaussian function, respectively. The appropriate bin width and bin number for each distribution are calculated based on the Freedman-Diaconis rule. The correlation between MAX-DOAS and satellite-retrieved monthly $NO_2$, $SO_2$, HCHO, and CHOCHO columns over Pantnagar is also shown.

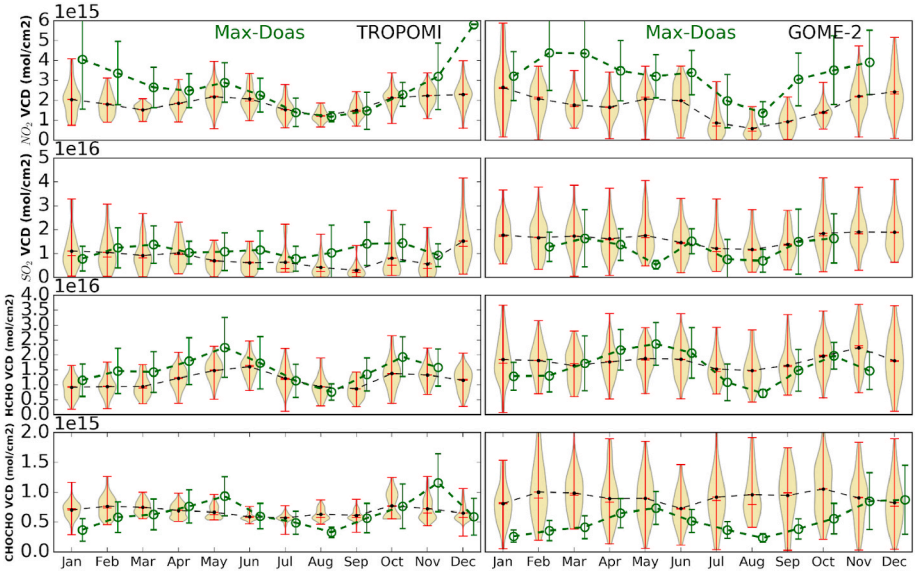


**Fig. 9.** Monthly variations of retrieved $NO_2$, $SO_2$, HCHO, and CHOCHO columns from Max-DOAS, TROPOMI, and GOME-2 observations in units of molecule/cm$^2$. MAX-DOAS observations are average for morning and the noontime overpass of the respective satellite. TROPOMI and GOME-2 observations are shown with a violin plot to emphasize their respective distribution better.

in the case of $SO_2$ and CHOCHO, they showed relatively poor monthly variations, and such features were also observed in MAX-DOAS. Additionally, the TROPOMI observations were more skewed towards their mean VCDs. At the same time, GOME-2 shows a higher spread in data around their mean VCDs which probably reflects the effect of coarse spatial resolution and limited collocations. The annual average $NO_2$ VCDs from TROPOMI and GOME-2 (Table 2) were lower by 32% and 48%, while $SO_2$ and HCHO VCDs were smaller in TROPOMI (33% and 20%) and larger in GOME-2 (33% and 12%). The average VCDs during the observation period show that even in morning overpass orbit, GOME-2 has not measured higher NO2 column and shows the possible contribution of the remote Himalaya in coarser resolution, which hinders the utilization of polar-orbiting satellites for intraday variabilities. However, geostationary satellites can be significantly utilized.

Additionally, compared to MAX-DOAS CHOCHO column the TROPOMI shows a relatively small positive bias of about 4%, whereas GOME-2 observation shows higher positive biases of about 75% (Table 2). Though there are well-captured observational features in satellites, there is still a notable difference that may be arising from the satellite retrieval apriories, influences from the nearby complex terrain

**Table 2**
Annual average VCDs of $NO_2$, $SO_2$, HCHO, and CHOCHO from TROPOMI, GOME-2, and respective MAX-DOAS observations. MAX-DOAS (M) corresponds to morning time and MAX-DOAS (A) corresponds to afternoon time observation of MAX-DOAS.

| Trace gases column (molecule/cm$^2$) | GOME-2 | MAX-DOAS (M) | TROPOMI | MAX-DOAS (A) |
|---|---|---|---|---|
| $NO_2$ | $1.7 \times 10^{15}$ | $3.3 \times 10^{15}$ | $1.9 \times 10^{15}$ | $2.8 \times 10^{15}$ |
| $SO_2$ | $1.6 \times 10^{16}$ | $1.2 \times 10^{16}$ | $0.8 \times 10^{16}$ | $1.1 \times 10^{16}$ |
| HCHO | $1.8 \times 10^{16}$ | $1.6 \times 10^{16}$ | $1.2 \times 10^{16}$ | $1.5 \times 10^{16}$ |
| CHOCHO | $0.91 \times 10^{15}$ | $0.52 \times 10^{15}$ | $0.68 \times 10^{15}$ | $0.65 \times 10^{15}$ |

of the Himalayas and different vertical sensitivities of the space-based sensors and MAX-DOAS. Also, space-based instruments have limited sensitivity close to the ground, where MAX-DOAS shows the highest sensitivity (Irie et al., 2008a; Kanaya et al., 2014). We further compared the intra-annual changes obtained for $NO_2$, $SO_2$, HCHO, and CHOCHO VCDs in the IGP foothill region (Fig. S5). Generally, no notable changes are observed in VCDs between 2017 and 2020, except slightly higher columns in 2018. Furthermore, the VCDs observation of $NO_2$ over Mohali (another IGP site) based on the MAX-DOAS observations reported an average concentration of $6.7 \times 10^{15}$ molecules cm$^{-2}$ (Kumar et al., 2020), which shows Mohali is 50% higher polluted in $NO_2$ scale compare to Pantnagar.

### 3.5. $R_{gf}$ variations and relationship with $NO_2$ column and EVI

The ratio of glyoxal to formaldehyde ($R_{gf}$) is often used to characterize the nature of VOCs precursors, the lower $R_{gf}$ values (<0.03) show mostly anthropogenic sources while larger $R_{gf}$ (>0.04) shows biogenic sources (Hoque et al., 2018a; Kaiser et al., 2015; Vrekoussis et al., 2010). Fig. 10 shows the diurnal variation of $R_{gf}$ and vertical profile. It shows a clear anthropogenic source of VOCs during the morning and evening hours, while dominant biogenic sources can be seen during noon hours when the temperature is higher (Fig. 10a). The vertical profile of $R_{gf}$ (Fig. 10b) shows mostly biogenic sources of VOCs at lower altitudes, while lesser $R_{gf}$ shows anthropogenic VOCs at higher altitudes.

Fig. 11 shows the monthly variation of $R_{gf}$ from MAX-DOAS, TROPOMI, and GOME-2. To better understand anthropogenic and biogenic influences on VOCs, we have also corroborated respective $NO_2$ VCDs and EVI (Fig. 11 black solid line) monthly variations over Pantnagar for 2017–2020 period. The average $R_{gf}$ over Pantnagar was 0.034 ± 0.010, 0.051 ± 0.008, and 0.061 ± 0.013 from MAX-DOAS, GOME-2, and TROPOMI, respectively. Different studies of $R_{gf}$ around different regions of the world typically reported $R_{gf}$ between 0.02 and 0.07 (e.g., DiGangi et al., 2012; Hoque et al., 2018a, 2018b; Kansal, 2009; MacDonald et al., 2012; Vrekoussis et al., 2009). The MAX-DOAS, GOME-2, and TROPOMI estimate of $R_{gf}$ mostly lay between 0.024 and 0.066, 0.039–0.065, and 0.037–0.081, respectively.

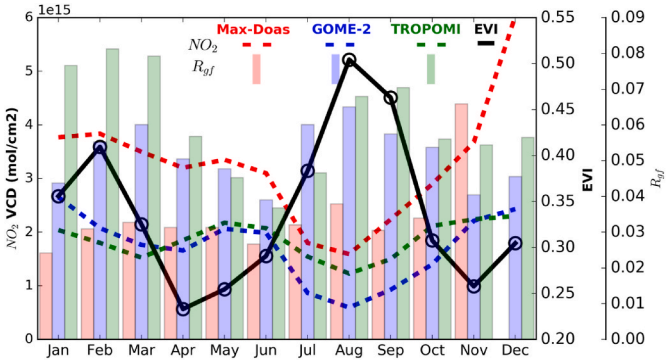


**Fig. 11.** $R_{gf}$ and $NO_2$ monthly variations from MAX-DOAS (red), TROPOMI (green), and GOME-2 (blue) observations, along with MODIS EVI (black color). The colored bar shows $R_{gf}$, and the thick dashed line shows $NO_2$ column observations from MAX-DOAS, TROPOMI, and GOME-2, respectively, in molecule/cm$^2$.

Furthermore, the MAX-DOAS $R_{gf}$ shows poor seasonality while satellite $R_{gf}$ shows opposite seasonality to $NO_2$ VCDs (signature of mostly biogenic sources of VOCs when less $NO_2$/anthropogenic emissions). Vrekoussis et al. (2009), based on GOME-2 measurements, reported dominant biogenic emissions of VOCs with high $R_{gf}$ between 0.04 and 0.06. In contrast, $R_{gf}$ below 0.03 were observed over regions with enhanced $NO_2$ levels or more anthropogenic sources, which also reported average $R_{gf}$ values of 0.042 ± 0.009 over India. Pantnagar, a Himalayan foothill region, shows a trade-off between the biogenic and anthropogenic sources of the VOCs during different seasons and requires more VOCs measurements like isoprene and monoterpenes. In contrast to satellite observation, which shows more biogenic sources, MAX-DOAS measurements were close to the transition regime (~0.03). Further, TROPOMI $R_{gf}$ is relatively higher, which might be due to afternoon overpasses of S–5P that are hours close to more biogenic emissions around the region (Fig. 11). At the same time, higher $R_{gf}$ in coarser-resolution GOME-2 may be contributed from the densely vegetated areas of the Himalayas. A similar overestimation of $R_{gf}$ by satellite measurements was also reported earlier with model-based $R_{gf}$ over the Indian region (Chutiya et al. 2019).

Additionally, a higher EVI (~0.5) is observed during the summer-monsoon and a relatively lower EVI (~0.25) during April and November. Fig. 12 shows the correlation between the EVI and HCHO (MAX-DOAS), EVI and CHOCHO (MAX-DOAS) over Pantnagar (Fig. 12). Both species are anti-correlated with the EVI at Pantnagar and indicate that the production of these OVOCs is not dominated by biogenic emissions and requires more VOCs observations. Such an anti-correlation is also seen with satellite HCHO observations (Fig. S6).

### 3.6. $R_{fn}$ variations and ozone production regimes

Fig. 13 shows the diurnal and monthly variation of $R_{fn}$. Usually, $R_{fn}$, the ratio between HCHO and $NO_2$, characterizes the ozone production

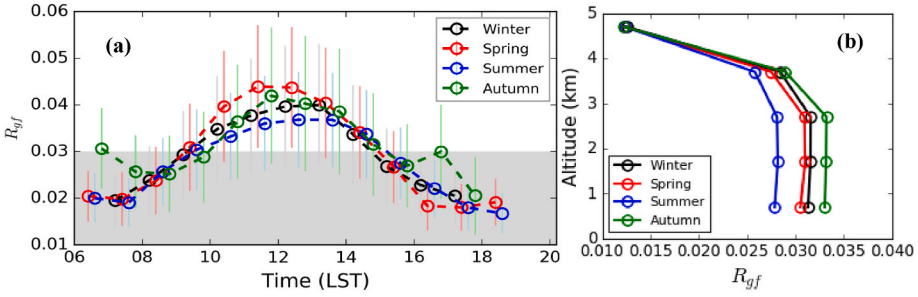


**Fig. 10.** (a) $R_{gf}$ diurnal variations over the foothill IGP site from MAX-DOAS observations near the surface and **(b)** $R_{gf}$ vertical profile.

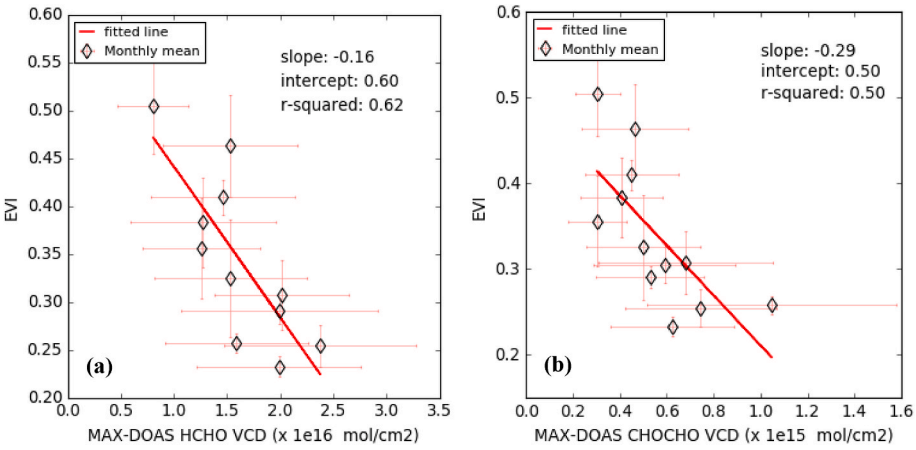


**Fig. 12.** Linear correlation between **(a)** HCHO/EVI and **(b)** CHOCHO/EVI from MAX-DOAS observations. The enhanced vegetation index (EVI) was taken from MODIS data of 250 m and 16 days of spatial and temporal resolution.

regime. Various studies (Duncan et al., 2010; Ojha et al., 2012; Peralta et al., 2021; Rawat and Naja, 2021) have characterized a region as a VOC-limited regime if HCHO/$NO_2$ ratio ($R_{fn}$) is less than 1.5, while $NO_x$ controls ozone production, ($NO_x$ limited) if HCHO/$NO_2$ ratio ($R_{fn}$) is greater than 2.3, and in between a transition regime is considered. $R_{fn}$ measurements over Pantnagar based on MAX-DOAS and satellite data show mostly $NO_x$-limited regimes for ozone production. The diurnal variation mostly shows a $NO_x$-limited regime with the highest $R_{fn}$ during autumn noon hours, except for winter, which shows a little VOC-limited or transition regime signature (Fig. 13a). The TROPOMI and MAX-DOAS monthly $R_{fn}$ variation also shows a little VOC-limited regime during winter, while a prominent $NO_x$-limited regime during the year can be seen. Further, TROPOMI and MAX-DOAS $R_{fn}$ values are comparable and follow similar monthly variations (Fig. 13b). However, GOME-2 over-estimated $R_{fn}$ values by more than two folds. Ojha et al. (2012), based on the box model simulations and in situ surface ozone observations, confirmed that the Pantnagar site falls under the $NO_x$-limited regime, and variation of different hydrocarbons played a minor role in affecting ozone levels.

## 4. Summary and conclusions

This study presents long-term (from January 2017 to December 2020) observations of $NO_2$, $SO_2$, HCHO, and CHOCHO at a foothill IGP site of the central Himalaya using a MAX-DOAS instrument and data from space-based sensors (TROPOMI and GOME-2). These trace gases exhibit a clear seasonal cycle near the surface with winter, spring, and autumn maxima and summer monsoon minima, depending on ambient meteorology and regional emissions. The larger emission sources and less $NO_x$ partitioning during winter divulges a higher $NO_2$ mixing ratio within the shallower boundary layer, while HCHO, and CHOCHO have higher concentrations during autumn months in 0–1 km layer. A similar seasonal cycle is also observed for the vertical profile of these trace gases, with most of the concentrations within the boundary layer (0–1 km). The diurnal variation in the lower troposphere shows a typical urban feature with higher concentrations during morning and evening hours for $NO_2$ and HCHO, while a noontime high is observed for CHOCHO. Furthermore, the diurnal rates of change for different seasons were comparable among the trace gases, with slightly higher photochemical activities in the spring and autumn seasons.

The wind rose diagram shows that the trace gases over the foothill IGP site depend significantly on winds and have few preferential wind direction sectors. Mainly transport along northwesterly winds seems to contribute to the ambient levels of the trace gases; however, during summer-monsoon and winter, influences from the southeasterly are also observed. Further, higher concentrations of $NO_2$ and CHOCHO were mostly seen for low wind speeds, implying local anthropogenic influence. In comparison, $SO_2$ and HCHO show higher concentrations even for high wind speeds and exhibit the possible role of transport.

MAX-DOAS is a useful tool for assessing satellite observation over a regionally representative urban/suburban site, like Pantnagar, where ground-based measurements are limited, and satellite observations can be significantly utilized after careful assessments. Knowing the potential of satellite observations, we have utilized the more advanced TROPOMI, an afternoon overpass, and GOME-2, a morning overpass satellite, to observe $NO_2$, $SO_2$, HCHO, and CHOCHO VCDs over a foothill IGP site. We observed annual mean tropospheric $NO_2$ vertical column densities (VCDs) of $3.2 \times 10^{15}$ (unit: molecules/$cm^2$), tropospheric $SO_2$ VCDs of $1.2 \times 10^{16}$, tropospheric HCHO VCDs of $1.6 \times 10^{16}$, and tropospheric CHOCHO VCDs of $0.6 \times 10^{15}$ from MAX-DOAS observations that are more-or-less similar, except for $NO_2$, to the annual mean values from TROPOMI ($1.9 \times 10^{15}$, $0.8 \times 10^{16}$, $1.2 \times 10^{16}$, $0.68 \times 10^{15}$) and GOME-2 ($1.7 \times 10^{15}$, $1.6 \times 10^{16}$, $1.8 \times 10^{16}$, $0.91 \times 10^{15}$), respectively. Both satellites measured a reasonable monthly variation of these trace gases with a slightly higher standard deviation in coarser resolution GOME-2. Higher VCDs in satellite are generally observed during winter, spring, and autumn, while lower VCDs are seen during the summer-monsoon, depending on ambient meteorology and regional emissions. The

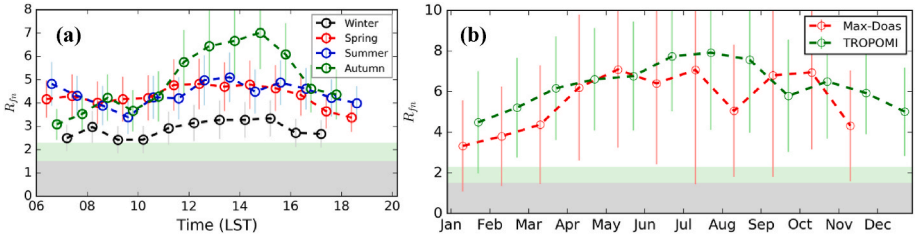


**Fig. 13.** (a) $R_{fn}$ diurnal variations observed at the foothill site from MAX-DOAS during four seasons. **(b)** $R_{fn}$ monthly variation from MAX-DOAS and TROPOMI measurements.

average VCDs during the observation period show that even in the morning overpass orbit, GOME-2 has not measured higher $NO_2$ concentration and shows the possible contribution of the remote Himalayas in coarser resolution. The histogram remainders of $NO_2$, $SO_2$, HCHO, and CHOCHO VCDs between TROPOMI/MAX-DOAS and GOME-2/MAX-DOAS show underestimation by more than $1 \times 10^{15}$ molecule/cm$^2$ for satellite retrieved $NO_2$ and $SO_2$ VCDs. In contrast, HCHO and CHOCHO VCDs show relatively small biases with underestimation in TROPOMI and overestimation in GOME-2 compared to MAX-DOAS.

Additionally, we have studied the possible VOCs sources and the ozone production regime over the foothill IGP site. Diurnal variation of $R_{gf}$ shows lower values during morning and evening hours, implying the anthropogenic sources of VOCs, while the influence of biogenic sources was seen during the noon hours. Further monthly variation of $R_{gf}$ shows mostly constant $R_{gf}$ from MAX-DOAS measurements in the range of 0.024–0.066, while higher $R_{gf}$ from TROPOMI and GOME-2, that notably anti-correlated with $NO_2$ VCDs and correlated with MODIS EVI data. The ozone production over the foothill IGP site is shown to be primarily controlled by $NO_x$ emission, while the role of VOCs seems to increase during the morning and evening hours of winter. To characterize the possible sources and factors influencing levels of environmentally important gases over IGP and nearby Himalayas, ground and space-based remote sensing observations are emerging as a valuable tool for better understanding. At the same time, their inter-comparison helps to divulge possible inhomogeneity between satellite and ground-based data and helps to demonstrate the possible differences and need for more accurate retrievals.

## Funding

This work was supported by ISRO-ATCTM project and ARIES Nainital.

## Data availability

The MAX-DOAS data is available on request. The S5P/TROPOMI L2 products are publicly available to users via the Copernicus Open Access Hub (last access: January 03, 2024). The GOME-2 data are publicly available via algorithm G2_L2_GLY version 1.0 by the DLR processing center in ftp server (ftp://acsaf.eoc.dlr.de/gome2b; last access: January 03, 2024). The ERA-5, MODIS fire data are publicly available via the Copernicus climate data store and Fire Information for Resource Management System (last access: January 03, 2024)

## CRediT authorship contribution statement

**Prajjwal Rawat:** Writing – original draft, Validation, Methodology, Investigation, Formal analysis, Data curation, Conceptualization. **Manish Naja:** Writing – review & editing, Validation, Supervision, Project administration, Methodology, Conceptualization. **Mahendar C. Rajwar:** Writing – review & editing, Validation, Methodology, Data curation. **H. Irie:** Writing – review & editing, Software, Methodology, Data curation. **Christophe Lerot:** Writing – review & editing, Methodology, Investigation. **Mukesh Kumar:** Writing – review & editing. **S. Lal:** Writing – review & editing, Investigation.

## Declaration of competing interest

The authors declare that they have no known competing financial interests or personal relationships that could have appeared to influence the work reported in this paper.

## Data availability

Data will be made available on request.

## Acknowledgement

This work is supported by ARIES, Ciba University, and the ISRO-ATCTM project. We are grateful to Director, ARIES and the Director, Biotech Bhavan, Haldi, for kindly supporting this work. We acknowledge ESA/EUMETSAT and ACSAF online data portals for providing TROPOMI and GOME label 2 data. We thank BIRA for providing the TROPOMI CHCHO data through the GLYRETRO project. We would also like to acknowledge the use of the MODIS fire and EVI data through FIRMS and NASA-EARTHDATA online data portals and the NOAA HYSPLIT model for backward air trajectory data. Technical support from Mr. Nitin and Deepak is highly appreciated.

## Appendix A. Supplementary data

Supplementary data to this article can be found online at https://doi.org/10.1016/j.atmosenv.2024.120746.

## References

Akimoto, H., 2003. Global air quality and pollution. Science 302 (5651), 1716–1719.
Beig, G., Ali, K., 2006. Behavior of boundary layer ozone and its precursors over a great alluvial plain of the world: Indo-Gangetic Plains. Geophys. Res. Lett. 33 (24). https://doi.org/10.1029/2006GL028352.
Beirle, S., Platt, U., Wenig, M., Wagner, T., 2003. Weekly cycle of NO 2 by GOME measurements: a signature of anthropogenic sources. Atmos. Chem. Phys. 3 (6), 2225–2232.
Belmonte Rivas, Stoffelen, A., 2019. Characterizing ERA-Interim and ERA5 surface wind biases using ASCAT. Ocean Sci. 15, 831–852. https://doi.org/10.5194/os-15-831-2019.
Bhardwaj, P., Naja, M., Kumar, R., Chandola, H.C., 2016. Seasonal, interannual, and long-term variabilities in biomass burning activity over South Asia. Environ. Sci. Pollut. Control Ser. 23 (5), 4397–4410.
Bhardwaj, P., Naja, M., Rupakheti, M., Lupascu, A., Mues, A., Panday, A.K., Kumar, R., Mahata, K.S., Lal, S., Chandola, H.C., Lawrence, M.G., 2018. Variations in surface ozone and carbon monoxide in the Kathmandu Valley and surrounding broader regions during SusKat-ABC field campaign: role of local and regional sources. Atmos. Chem. Phys. 18 (16), 11949–11971.
Bianchi, F., Junninen, H., Bigi, A., Sinclair, V.A., Dada, L., Hoyle, C.R., Zha, Q., Yao, L., Ahonen, L.R., Bonasoni, P., Mazon, S.B., 2021. Biogenic particles formed in the Himalaya as an important source of free tropospheric aerosols. Nat. Geosci. 14 (1), 4–9.
Biswas, M.S., Pandithurai, G., Aslam, M.Y., Patil, R.D., Anilkumar, V., Dudhambe, S.D., Lerot, C., De Smedt, I., Van Roozendael, M., Mahajan, A.S., 2020. Effect of boundary layer evolution on nitrogen dioxide (NO2) and formaldehyde (HCHO) concentrations at a high-altitude observatory in western India. Aerosol Air Qual. Res. 21, 200193 https://doi.org/10.4209/aaqr.2020.05.0193.
Biswas, M.S., Mahajan, A.S., 2021. Year-longconcurrent MAX-DOAS observations of nitrogen dioxide and formaldehyde at pune: understanding diurnal and seasonal variation drivers. Aerosol Air Qual. Res. 21, 200524. https://doi.org/10.4209/aaqr.200524.
Bonasoni, P., Laj, P., Marinoni, A., Sprenger, M., Angelini, F., Arduini, J., Bonafè, U., Calzolari, F., Colombo, T., Decesari, S., Biagio, C.D., 2010. Atmospheric Brown Clouds in the Himalayas: first two years of continuous observations at the Nepal Climate Observatory-Pyramid (5079 m). Atmos. Chem. Phys. 10 (15), 7515–7531.
Burrows, J.P., Weber, M., Buchwitz, M., Rozanov, V., Ladstätter-Weißenmayer, A., Richter, A., DeBeek, R., Hoogen, R., Bramstedt, K., Eichmann, K.U., Eisinger, M., 1999. The global ozone monitoring experiment (GOME): mission concept and first scientific results. J. Atmos. Sci. 56 (2), 151–175.
Chen, T.M., Kuschner, W.G., Gokhale, J., Shofer, S., 2007. Outdoor air pollution: nitrogen dioxide, sulfur dioxide, and carbon monoxide health effects. Am. J. Med. Sci. 333 (4), 249–256.
Chutia, L., Ojha, N., Girach, I.A., Sahu, L.K., Alvarado, L.M., Burrows, J.P., Pathak, B., Bhuyan, P.K., 2019. Distribution of volatile organic compounds over Indian subcontinent during winter: WRF-chem simulation versus observations. Environ. Pollut. 252, 256–269.
De Smedt, I., Van Roozendael, M., Stavrakou, T., Müller, J.-F., Lerot, C., Theys, N., Valks, P., Hao, N., van der A, R., 2012. Improved retrieval of global tropospheric formaldehyde columns from GOME-2/MetOp-A addressing noise reduction and instrumental degradation issues. Atmos. Meas. Tech. 5, 2933–2949. https://doi.org/10.5194/amt-5-2933-2012.
De Smedt, I., Pinardi, G., Vigouroux, C., Compernolle, S., Bais, A., Benavent, N., Boersma, F., Chan, K.L., Donner, S., Eichmann, K.U., Hedelt, P., 2021. Comparative assessment of TROPOMI and OMI formaldehyde observations and validation against MAX-DOAS network column measurements. Atmos. Chem. Phys. 21 (16), 12561–12593.
DiGangi, J.P., Henry, S.B., Kammrath, A., Boyle, E.S., Kaser, L., Schnitzhofer, R., Graus, M., Turnipseed, A., Park, J.H., Weber, R.J., Hornbrook, R.S., 2012. Observations of glyoxal and formaldehyde as metrics for the anthropogenic impact on rural photochemistry. Atmos. Chem. Phys. 12 (20), 9529–9543.

Duncan, B.N., Yoshida, Y., Olson, J.R., Sillman, S., Martin, R.V., Lamsal, L., Hu, Y., Pickering, K.E., Retscher, C., Allen, D.J., Crawford, J.H., 2010. Application of OMI observations to a space-based indicator of NOx and VOC controls on surface ozone formation. Atmos. Environ. 44 (18), 2213–2223.

Fu, P., Kawamura, K., Chen, J., Barrie, L.A., 2009. Isoprene, monoterpene, and sesquiterpene oxidation products in the high Arctic aerosols during late winter to early summer. Environ. Sci. Technol. 43 (11), 4022–4028.

Gilbert, N.L., Woodhouse, S., Stieb, D.M., Brook, J.R., 2003. Ambient nitrogen dioxide and distance from a major highway. Sci. Total Environ. 312 (1–3), 43–46.

Griffin, D., Zhao, X., McLinden, C.A., Boersma, F., Bourassa, A., Dammers, E., Degenstein, D., Eskes, H., Fehr, L., Fioletov, V., Hayden, K., 2019. High-resolution mapping of nitrogen dioxide with TROPOMI: first results and validation over the Canadian oil sands. Geophys. Res. Lett. 46 (2), 1049–1060.

Ghude, S.D., Fadnavis, S., Beig, G., Polade, S.D., Van Der A, R.J., 2008. Detection of surface emission hot spots, trends, and seasonal cycle from satellite-retrieved NO2 over India. J. Geophys. Res. Atmos. 113 (D20).

Henry, S.B., DiGangi, J.P., Weber, R.J., Gentner, D.R., Goldstein, A.H., Keutsch, F.N., 2012. Formaldehyde Influences from Combustion and Photochemistry at a California Urban Site. preparation.

Hoque, H.M.S., Irie, H., Damiani, A., Rawat, P., Naja, M., 2018a. First simultaneous observations of formaldehyde and glyoxal by MAX-DOAS in the Indo-Gangetic Plain region. Inside Solaris 14, 159–164.

Hoque, H.M.S., Irie, H., Damiani, A., 2018b. First MAX-DOAS observations of formaldehyde and glyoxal in phimai, Thailand. J. Geophys. Res. Atmos. 123 (17), 9957–9975.

Hong, Q., Liu, C., Hu, Q., Xing, C., Tan, W., Liu, T., Liu, J., 2021. Vertical distributions of tropospheric SO2 based on MAX-DOAS observations: investigating the impacts of regional transport at different heights in the boundary layer. J. Environ. Sci. 103, 119–134.

Hönninger, G., Platt, U., 2002. Observations of BrO and its vertical distribution during surface ozone depletion at Alert. Atmos. Environ. 36 (15–16), 2481–2489.

Hönninger, G., Friedeburg, C.V., Platt, U., 2004. Multi-axis differential optical absorption spectroscopy (MAX-DOAS). Atmos. Chem. Phys. 4 (1), 231–254.

Igarashi, Y., Sawa, Y., Yoshioka, K., Takahashi, H., Matsueda, H., Dokiya, Y., 2006. Seasonal variations in SO2 plume transport over Japan: observations at the summit of Mt. Fuji from winter to summer. Atmos. Environ. 40 (36), 7018–7033.

Irie, H., Kanaya, Y., Akimoto, H., Tanimoto, H., Wang, Z., Gleason, J.F., Bucsela, E.J., 2008a. Validation of OMI tropospheric NO2 column data using MAX-DOAS measurements deep inside the north China plain in june 2006: mount tai experiment 2006. Atmos. Chem. Phys. 8 (22), 6577–6586.

Irie, H., Kanaya, Y., Akimoto, H., Iwabuchi, H., Shimizu, A., Aoki, K., 2008b. First retrieval of tropospheric aerosol profiles using MAX-DOAS and comparison with lidar and sky radiometer measurements. Atmos. Chem. Phys. 8 (2), 341–350.

Irie, H., Takashima, H., Kanaya, Y., Boersma, K.F., Gast, L., Wittrock, F., Brunner, D., Zhou, Y., Roozendael, M.V., 2011. Eight-component retrievals from ground-based MAX-DOAS observations. Atmos. Meas. Tech. 4 (6), 1027–1044.

Irie, H., Nakayama, T., Shimizu, A., Yamazaki, A., Nagai, T., Uchiyama, A., Zaizen, Y., Kagamitani, S., Matsumi, Y., 2015. Evaluation of MAX-DOAS aerosol retrievals by coincident observations using CRDS, lidar, and sky radiometer inTsukuba, Japan. Atmos. Meas. Tech. 8 (7), 2775–2788.

Irie, H., Hoque, H.M.S., Damiani, A., Okamoto, H., Fatmi, A.M., Khatri, P., Takamura, T., Jarupongsakul, T., 2019. Simultaneous observations by sky radiometer and MAX-DOAS for characterization of biomass burning plumes in central Thailand in January–April 2016. Atmos. Meas. Tech. 12 (1), 599–606.

Jena, C., Ghude, S.D., Beig, G., Chate, D.M., Kumar, R., Pfister, G.G., Lal, D.M., Surendran, D.E., Fadnavis, S., 2015. Inter-comparison of different NOx emission inventories and associated variation in simulated surface ozone in Indian region. Atmos. Environ. 117, 61–73.

Kaiser, R.H., Andrews-Hanna, J.R., Wager, T.D., Pizzagalli, D.A., 2015. Large-scale network dysfunction in major depressive disorder: a meta-analysis of resting-state functional connectivity. JAMA Psychiatr. 72 (6), 603–611.

Kanaya, Y., Irie, H., Takashima, H., Iwabuchi, H., Akimoto, H., Sudo, K., Gu, M., Chong, J., Kim, Y.J., Lee, H., Li, A., 2014. Long-term MAX-DOAS network observations of NO 2 in Russia and Asia (MADRAS) during the period 2007–2012: instrumentation, elucidation of climatology, and comparisons with OMI satellite observations and global model simulations. Atmos. Chem. Phys. 14 (15), 7909–7927.

Kansal, A., 2009. Sources and reactivity of NMHCs and VOCs in the atmosphere: a review. J. Hazard Mater. 166 (1), 17–26.

Kim, S., Karl, T., Guenther, A., Tyndall, G., Orlando, J., Harley, P., Rasmussen, R., Apel, E., 2010. Emissions and ambient distri- butions of Biogenic Volatile Organic Compounds (BVOC) in a ponderosa pine ecosystem: interpretation of PTR-MS mass spectra. Atmos. Chem. Phys. 10, 1759–1771. https://doi.org/10.5194/acp-10-1759-2010.

Koppmann, R., von Czapiewski, K., Reid, J.S., 2005. A review of biomass burning emissions, part I: gaseous emissions of carbon monoxide, methane, volatile organic compounds, and nitrogen containing compounds. Atmos. Chem. Phys. Discuss. 5, 10455–10516. https://doi.org/10.5194/acpd-5-10455-2005.

Kumar, R., Naja, M., Venkataramani, S., Wild, O., 2010. Variations in surface ozone at Nainital: a high-altitude site in the central Himalayas. J. Geophys. Res. Atmos. 115 (D16).

Kumar, V., Beirle, S., Dörner, S., Mishra, A.K., Donner, S., Wang, Y., Sinha, V., Wagner, T., 2020. Long-term MAX-DOAS measurements of NO 2, HCHO, and aerosols and evaluation of corresponding satellite data products over Mohali in the Indo-Gangetic Plain. Atmos. Chem. Phys. 20 (22), 14183–14235.

Lerot, C., Hendrick, F., Van Roozendael, M., Alvarado, L., Richter, A., De Smedt, I., Theys, N., Vlietinck, J., Yu, H., Van Gent, J., Stavrakou, T., 2021. Glyoxal tropospheric column retrievals from TROPOMI, multi-satellite intercomparison and ground-based validation. Atmospheric Measurement Techniques Discussions 1–48.

Li, C., McLinden, C., Fioletov, V., Krotkov, N., Carn, S., Joiner, J., Streets, D., He, H., Ren, X., Li, Z., Dickerson, R.R., 2017. India is overtaking China as the world's largest emitter of anthropogenic sulfur dioxide. Sci. Rep. 7 (1), 1–7.

Lin, W., Xu, X., Zhang, X., Tang, J., 2008. Contributions of pollutants from north China plain to surface ozone at the shangdianzi GAW station. Atmos. Chem. Phys. 8 (19), 5889–5898.

Long, S., Wei, X., Zhang, F., Zhang, R., Xu, J., Wu, K., Li, Q., Li, W., 2022. Estimating daily ground-level NO2 concentrations over China based on TROPOMI observations and machine learning approach. Atmos. Environ. 289, 119310 https://doi.org/10.1016/j.atmosenv.2022.119310.

Lowe, D.C., Schmidt, U., 1983. Formaldehyde (HCHO) measurements in the nonurban atmosphere. J. Geophys. Res.: Oceans 88 (C15), 10844–10858. https://doi.org/10.1029/JC088iC15p10844.

MacDonald, S.M., Oetjen, H., Mahajan, A.S., Whalley, L.K., Edwards, P.M., Heard, D.E., Jones, C.E., Plane, J.M.C., 2012. DOAS measurements of formaldehyde and glyoxal above a south-east Asian tropical rainforest. Atmos. Chem. Phys. 12 (13), 5949–5962.

Mallik, C., Lal, S., 2014. Seasonal characteristics of $SO_2$, $NO_2$, and CO emissions in and around the Indo-Gangetic Plain. Environ. Monit. Assess. 186, 1295–1310. https://doi.org/10.1007/s10661-013-3458-y.

Mallik, C., Lal, S., Venkataramani, S., 2015. Trace gases at a semi-arid urban site in western India: variability and inter-correlations. J. Atmos. Chem. 72 (2), 143–164.

Mauzerall, D.L., Wang, X.P., 2001. Protecting agricultural crops from the effects of tropospheric ozone exposure: reconciling science and standard setting in the United States, Europe, and Asia. Annu. Rev. Energy Environ. 26, 237–268.

McMichael, A.J., Woodruff, R.E., Hales, S., 2006. Climate change and human health: present and future risks. Lancet 367 (9513), 859–869.

Munro, R., Lang, R., Klaes, D., Poli, G., Retscher, C., Lindstrot, R., Huckle, R., Lacan, A., Grzegorski, M., Holdak, A., Kokhanovsky, A., 2016. The GOME-2 instrument on the Metop series of satellites: instrument design, calibration, and level 1 data processing–an overview. Atmos. Meas. Tech. 9 (3), 1279–1301.

Naja, M., Mallik, C., Sarangi, T., Sheel, V., Lal, S., 2014. SO2 measurements at a high altitude site in the central Himalayas: role of regional transport. Atmos. Environ. 99, 392–402.

Ojha, N., Naja, M., Singh, K.P., Sarangi, T., Kumar, R., Lal, S., Lawrence, M.G., Butler, T. M., Chandola, H.C., 2012. Variabilities in ozone at a semi-urban site in the Indo-Gangetic Plain region: association with the meteorology and regional processes. J. Geophys. Res. Atmos. 117 (D20).

Ojha, N., Pozzer, A., Akritidis, D., Lelieveld, J., 2017. Secondary ozone peaks in the troposphere over the Himalayas. Atmos. Chem. Phys. 17 (11), 6743–6757.

Park, M., Randel, W.J., Emmons, L.K., Livesey, N.J., 2009. Transport pathways of carbon monoxide in the Asian summer monsoon diagnosed from Model of Ozone and Related Tracers (MOZART). J. Geophys. Res. Atmos. 114 (D8).

Patz, J.A., Campbell-Lendrum, D., Holloway, T., Foley, J.A., 2005. Impact of regional climate change on human health. Nature 438 (7066), 310–317.

Peralta, O., Ortínez-Alvarez, A., Torres-Jardón, R., Suárez-Lastra, M., Castro, T., Ruíz-Suárez, L.G., 2021. Ozone over Mexico City during the COVID-19 pandemic. Sci. Total Environ. 761, 143183.

Peters, E., Wittrock, F., Großmann, K., Frieß, U., Richter, A., Burrows, J.P., 2012. Formaldehyde and nitrogen dioxide over the remote western Pacific Ocean: SCIAMACHY and GOME-2 validation using ship-based MAX-DOAS observations. Atmos. Chem. Phys. 12 (22), 11179–11197.

Platt, U., Stutz, J., 2008. Differential absorption spectroscopy. In: Differential Optical Absorption Spectroscopy. Springer, Berlin, Heidelberg, pp. 135–174.

Rajwar, M.C., Naja, M., Srivastava, P., Tiwari, R.K., Venkataramani, S., Lal, S., 2024. Online observation of light non-methane hydrocarbons (C2–C5) over the central Himalayas: influence of the Indo-Gangetic Plain region. Atmos. Pollut. Res., 102078

Ramanathan, V.C.P.J., Crutzen, P.J., Kiehl, J.T., Rosenfeld, D., 2001. Aerosols, climate, and the hydrological cycle. Science 294 (5549), 2119–2124.

Ravishankara, A.R., David, L.M., Pierce, J.R., Venkataraman, C., 2020. Outdoor air pollution in India is not only an urban problem. Proc. Natl. Acad. Sci. USA 117 (46), 28640–28644.

Rawat, P., Naja, M., 2021. Remote sensing study of ozone, NO2, and CO: some contrary effects of SARS-CoV-2 lockdown over India. Environ. Sci. Pollut. Res. https://doi.org/10.1007/s11356-021-17441-2.

Richter, A., Burrows, J., 2002. Tropospheric NO2 from GOME measurements. Adv. Space Res. 29, 1673–1683.

Saud, T., Mandal, T.K., Gadi, R., Singh, D.P., Sharma, S.K., Saxena, M., Mukherjee, A., 2011. Emission estimates of particulate matter (PM) and trace gases (SO2, NO and NO2) from biomass fuels used in rural sector of Indo-Gangetic Plain, India. Atmos. Environ. 45 (32), 5913–5923.

Shaiganfar, R., Beirle, S., Sharma, M., Chauhan, A., Singh, R.P., Wagner, T., 2011. Estimation of NO x emissions from Delhi using Car MAX-DOAS observations and comparison with OMI satellite data. Atmos. Chem. Phys. 11 (21), 10871–10887.

Sharma, A.R., Kharol, S.K., Badarinath, K.V.S., Singh, D., 2010. Impact of agriculture crop residue burning on atmospheric aerosol loading–a study over Punjab State, India. In: Annales Geophysicae, vol. 28. Copernicus GmbH, pp. 367–379, 2.

Singh, N., Banerjee, T., Raju, M.P., Deboudt, K., Sorek-Hamer, M., Singh, R.S., Mall, R.K., 2018. Aerosol chemistry, transport, and climatic implications during extreme biomass burning emissions over the Indo-Gangetic Plain. Atmos. Chem. Phys. 18 (19), 14197–14215.

Sinha, V., Kumar, V., Sarkar, C., 2014. Chemical composition of pre-monsoon air in the Indo-Gangetic Plain measured using a new air quality facility and PTR-MS: high surface ozone and strong influence of biomass burning. Atmos. Chem. Phys. 14 (12), 5921–5941.

Spurr, R., et al., 2010. GOME-2 Trace Gas Column Retrievals: Optimized Wavelengths for the O3 AMF, Final Report. O3MSAF-VS project.

Srivastava, A.K., Thomas, A., Hooda, R.K., Kanawade, V.P., Hyvärinen, A.P., Bisht, D.S., Tiwari, S., 2021. How secondary inorganic aerosols from Delhi influence aerosol optical and radiative properties at a downwind sub-urban site over Indo-Gangetic Basin? Atmos. Environ. 248, 118246.

Surl, L., Palmer, P.I., González Abad, G., 2018. Which processes drive observed variations of HCHO columns over India? Atmos. Chem. Phys. 18 (7), 4549–4566.

Theys, N., Smedt, I.D., Yu, H., Danckaert, T., Gent, J.V., Hörmann, C., Wagner, T., Hedelt, P., Bauer, H., Romahn, F., Pedergnana, M., 2017. Sulfur dioxide retrievals from TROPOMI onboard Sentinel-5 Precursor: algorithm theoretical basis. Atmos. Meas. Tech. 10 (1), 119–153.

Tirpitz, J.L., Frieß, U., Hendrick, F., Alberti, C., Allaart, M., Apituley, A., Bais, A., Beirle, S., Berkhout, S., Bognar, K., Bösch, T., 2020. Intercomparison of MAX-DOAS vertical profile retrieval algorithms: studies on field data from the CINDI-2 campaign. Atmospheric Measurement Techniques Discussions 2020, 1–49.

Valks, P., Pinardi, G., Richter, A., Lambert, J.C., Hao, N., Loyola, D., Roozendael, M.V., Emmadi, S., 2011. Operational total and tropospheric NO 2 column retrieval for GOME-2. Atmos. Meas. Tech. 4 (7), 1491–1514.

Van Der Werf, G.R., Randerson, J.T., Giglio, L., Van Leeuwen, T.T., Chen, Y., Rogers, B. M., Mu, M., Van Marle, M.J., Morton, D.C., Collatz, G.J., Yokelson, R.J., 2017. Global fire emissions estimates during 1997–2016. Earth Syst. Sci. Data 9 (2), 697–720.

Van Geffen, J., Boersma, K.F., Eskes, H., Sneep, M., Ter Linden, M., Zara, M., Veefkind, J. P., 2020. S5P TROPOMI NO2 slant column retrieval: method, stability, uncertainties and comparisons with OMI. Atmos. Meas. Tech. 13 (3), 1315–1335.

Veefkind, J.P., Aben, I., McMullan, K., Förster, H., De Vries, J., Otter, G., Claas, J., Eskes, H.J., De Haan, J.F., Kleipool, Q., Van Weele, M., 2012. TROPOMI on the ESA Sentinel-5 Precursor: a GMES mission for global observations of the atmospheric composition for climate, air quality and ozone layer applications. Rem. Sens. Environ. 120, 70–83.

Verhoelst, T., Compernolle, S., Pinardi, G., Lambert, J.C., Eskes, H.J., Eichmann, K.U., Fjæraa, A.M., Granville, J., Niemeijer, S., Cede, A., Tiefengraber, M., 2021. Ground-based validation of the Copernicus Sentinel-5p TROPOMI NO 2 measurements with the NDACC ZSL-DOAS, MAX-DOAS and Pandonia global networks. Atmos. Meas. Tech. 14 (1), 481–510.

Venzac, H., Sellegri, K., Laj, P., Villani, P., Bonasoni, P., Marinoni, A., Cristofanelli, P., Calzolari, F., Fuzzi, S., Decesari, S., Facchini, M.C., 2008. High frequency new particle formation in the Himalayas. Proc. Natl. Acad. Sci. USA 105 (41), 15666–15671.

Vigouroux, C., Langerock, B., Bauer Aquino, C.A., Blumenstock, T., Cheng, Z., De Mazière, M., De Smedt, I., Grutter, M., Hannigan, J.W., Jones, N., Kivi, R., 2020. TROPOMI–Sentinel-5 Precursor formaldehyde validation using an extensive network of ground-based Fourier-transform infrared stations. Atmos. Meas. Tech. 13 (7), 3751–3767.

Volkamer, R., San Martini, F., Molina, L.T., Salcedo, D., Jimenez, J.L., Molina, M.J., 2007. A missing sink for gas-phase glyoxal in Mexico City: Formation of secondary organic aerosol. Geophys. Res. Lett. 34 (19).

Vrekoussis, M., Wittrock, F., Richter, A., Burrows, J.P., 2009. Temporal and spatial variability of glyoxal as observed from space. Atmos. Chem. Phys. 9 (13), 4485–4504.

Wagner, T., Dix, B.V., Friedeburg, C.V., Frieß, U., Sanghavi, S., Sinreich, R., Platt, U., 2004. MAX-DOAS O4 measurements: a new technique to derive information on atmospheric aerosols—principles and information content. J. Geophys. Res. Atmos. 109 (D22).

Wang, Y., Jacob, D.J., 1998. Anthropogenic forcing on tropospheric ozone and OH since preindustrial times. J. Geophys. Res. Atmos. 103 (D23), 31123–31135.

Wang, Y., Yuan, Q., Li, T., Zhu, L., Zhang, L., 2021. Estimating daily full-coverage near surface O3, CO, and NO2 concentrations at a high spatial resolution over China based on S5P-TROPOMI and GEOS-FP. ISPRS J. Photogrammetry Remote Sens. 175, 311–325. https://doi.org/10.1016/j.isprsjprs.2021.03.018.

Xing, C., Liu, C., Hu, Q., Fu, Q., Lin, H., Wang, S., Su, W., Wang, W., Javed, Z., Liu, J., 2020. Identifying the wintertime sources of volatile organic compounds (VOCs) from MAX-DOAS measured formaldehyde and glyoxal in Chongqing, southwest China. Sci. Total Environ. 715, 136258.

Zhu, S., Xu, J., Fan, M., Yu, C., Letu, H., Zeng, Q., Zhu, H., Wang, H., Wang, Y., Shi, J., 2023. Estimating near-surface concentrations of major air pollutants from space: a universal estimation framework lapso. IEEE Trans. Geosci. Rem. Sens. 61, 1–11. https://doi.org/10.1109/TGRS.2023.3248180.